ARTICLE

Microstructural and Photoconversion Efficiency Enhancement of Compact Films of Lead-Free Perovskite Derivative $Rb_3Sb_2I_9$†

Fengzhu Li,‡[a] Yan Wang,[a] Kai Xia,[a] Robert L. Z. Hoye,[b] Vincenzo Pecunia‡[a*]

DOI: 10.1039/C9TA13352F

Abstract

While lead-based perovskites have held center stage in photovoltaic and optoelectronic research over the past decade, their toxicity has raised significant concerns, spurring the search for lead-free alternatives with similar potential. While a number of lead-free antimony-/bismuth-based compounds have been proposed, they have typically exhibited limited charge extraction efficiency, which has prompted the widespread adoption of a mesoporous device architecture. With a focus on compact films of $Rb_3Sb_2I_9$—an emerging lead-free two-dimensional perovskite derivative—this study presents two strategies to enhance their microstructure: one relying on the reduction of the supersaturation level during the annealing step, and the other involving high-temperature annealing in an SbI_3 atmosphere. Both strategies lead to a considerable improvement in film morphology and microstructure, with a twofold increase in apparent grain size. Such high-quality compact films deliver a pronounced rise in external quantum efficiency, as well as in short-circuit photocurrent under solar illumination—all this without the aid of a mesoporous architecture for charge extraction. Hall effect and photocurrent-power characterization show that this performance improvement results from an increase in charge carrier mobility and a reduction in the number of recombination centers. The microstructural improvement, photoconversion effiency boost, and mechanistic insight provide valuable indications on the status and prospects of $Rb_3Sb_2I_9$ and related derivatives—as relevant to the future exploration of these compounds for lead-free top-cells in tandem photovoltaics, indoor photovoltaics, and other optoelectronic application domains.

Introduction

In recent years lead-halide perovskites have emerged as a class of semiconductors with outstanding optoelectronic properties.[1–7] Importantly, they are particularly attractive for low-cost and high-performance photovoltaics,[8–10] in view of their power conversion efficiency (PCE) in single-cell devices now exceeding 25%[11] and due to their facile solution processability.[12–14] The toxicity of lead, however, is a major obstacle to their large-scale commercialization.[15–17] This has prompted the search for materials that are chemically, crystallographically or electronically similar to lead-halide perovskites while being lead-free.[18,19] This search is relevant to the identification of alternatives not only for single-cell devices for solar harvesting, but also for multi-junctions photovoltaics, indoor photovoltaics, photocathodes for water splitting, and other optoelectronic application domains such as photodetection.[20–26] Insight from studies on lead-based perovskites suggests that other potentially promising halide perovskites should rely on a large highly-polarizable metal cation featuring n*s* outer orbitals that can hybridize with halogen *p* orbitals.[18,27] An emerging approach to lead replacement involves antimony, which yields Sb^{3+} cations that, like Pb^{2+}, have stable valence s^2 electrons and comparable ionic radii. This has led investigators to consider a number of ternary antimony-iodide perovskite derivatives (ASbIs), i.e., materials of general formula $A_3Sb_2I_9$, with A being a monovalent cation.[28,29] Structurally, ASbIs come in two forms: as zero-dimensional (0D) derivatives (e.g., A = $CH_3NH_3^+$ or Cs^+), featuring isolated face-sharing $[Sb_2X_9]^{3-}$ bioctahedra; and as two-dimensional (2D) derivatives (e.g., A = K^+, Rb^+, or Cs^+), featuring planes of corner-sharing $[SbI_6]^{3-}$ octahedra. [30] A 2D structure has been regarded as more promising for ASbI photovoltaics, because charge transport is expected to be facilitated within the planes of $[SbI_6]^{3-}$ octahedra. While $Cs_3Sb_2I_9$ may form a 2D structure,[31] it can only do so through dedicated processing protocols.[32–34] By contrast, $K_3Sb_2I_9$ and $Rb_3Sb_2I_9$ intrinsically adopt a stable 2D structure.[35] Finally, in addition to its favorable and stable 2D structure, it has been shown that $Rb_3Sb_2I_9$ is the only ASbI with a direct bandgap, and it is also the ASbI with the smallest exciton binding energy ($\approx$100 meV).[35,36]

Material considerations suggest that $Rb_3Sb_2I_9$ has considerable photovoltaic potential, especially in regard to its use for top-cells in tandem photovoltaics and for indoor photovoltaics. Interestingly, this compound has received little attention to date. The first study on the synthesis and photovoltaic application of this material reports a power conversion efficiency (PCE) of 0.66%, along with a peak external quantum efficiency (EQE) of 29% (at short circuit).[36] Adopting similar deposition processes, Correa-Baena et al. later reported a champion PCE of 0.76%,[35] while most recently Weber et al.

[a] *Institute of Functional Nano & Soft Materials (FUNSOM), Jiangsu Key Laboratory for Carbon-Based Functional Materials & Devices, Soochow University, 199 Ren'ai Road, Suzhou, 215123, Jiangsu, PR China. E-mail: vp293@suda.edu.cn*

[b] *Department of Materials, Imperial College London, Exhibition Road, London SW7 2AZ, United Kingdom.*

†Electronic Supplementary Information (ESI) available: details on deposition processes; relationship between supersaturation and grain size; absorption properties; photoelectron spectroscopy; double-sweep photovoltaic plots and distribution of photovoltaic parameters; key photovoltaic parameters from relevant literature. See DOI: 10.1039/x0xx00000x

‡ F. L. and V. P. contributed equally to this work.

achieved a PCE of 1.37%.[37] Interestingly, the more-than-twofold increase in PCE of the latter work comes with a slightly lower EQE (26%).[37] It is noteworthy that all these studies adopt a device architecture in which $Rb_3Sb_2I_9$ is grown on (and partly embedded in) a mesoporous electron transport layer. In fact, the adoption of a mesoporous device architecture has been mainstream in works on antimony-halide and bismuth-halide perovskite derivatives to date, typically in view of the presumed limitation in charge-extraction efficiency of such compounds. Indeed, a mesoporous architecture has been demonstrated to improve the photoconversion efficiency (hence, the EQE and short-circuit photocurrent) of absorbers that otherwise suffer from limited charge-extraction efficiency in compact thin-film form.[38,39]

In the broader perovskite photovoltaics research landscape, it has generally been observed that the morphology of a polycrystalline perovskite layer has considerable impact on its optoelectronic/photovoltaic properties.[40,41] Importantly, larger grain sizes have been found to lead to larger carrier mobilities and lifetimes, both of which boost the photoconversion efficiency by synergistically extending carrier drift/diffusion length.[42–46] In fact, the highest performance of lead-based-perovskite solar cells has been attained with films featuring a grain size in the region of 1 μm or larger.[1,2] As a term of comparison, the maximum apparent grain size of the $Rb_3Sb_2I_9$ films in the literature to date is in the region of 200 nm.[36]

In this study we harness compact films of $Rb_3Sb_2I_9$ towards enhanced optoelectronic performance and provide fresh insight into its photoconversion and photovoltaic potential as a promising lead-free perovskite. We achieve this by firstly developing deposition strategies that lead to compact polycrystalline $Rb_3Sb_2I_9$ thin films with considerable improvement in microstructure. In order to assess the inherent optoelectronic potential of $Rb_3Sb_2I_9$, we then characterize these high-quality films as compact photoactive layers within a planar device structure. Doing without the aid of a mesoporous transport layer for charge extraction, we are thus able to unravel how the intrinsic optoelectronic properties of high-quality polycrystalline $Rb_3Sb_2I_9$ films impact their photoconversion and photovoltaic performance. Additionally, through photocurrent-power characterization and Hall effect measurements, we are able to rationalize the observed device performance, and identify the future potential of $Rb_3Sb_2I_9$ as a lead-free optoelectronic and photovoltaic material.

Results and discussion

With the aim of gaining insight into the impact of morphology on the intrinsic optoelectronic and photovoltaic properties of $Rb_3Sb_2I_9$, we investigated several strategies to deposit high-quality compact $Rb_3Sb_2I_9$ films on a planar substrate. As a first step, we evaluated the conventional process (CP) previously adopted in the literature for the deposition of $Rb_3Sb_2I_9$ on a mesoporous substrate. While based on the mainstream antisolvent method, CP differs insofar as the antisolvent (toluene) incorporates a small amount of SbI_3 to compensate for iodine deficiency in the film being formed (**Figure 1a**). In CP, spin coating is followed by a straightforward hotplate annealing step at 120 °C. (See the Experimental Section and **Figure S1** for further details.)

During the formation of a perovskite film via solution-based methods, grain growth dynamically competes with nucleation to determine the final grain size in the dry film. This competition is controlled by the local supersaturation level, with higher values leading to faster nucleation and smaller grain size (**Figure S2**). Following this lead, we investigated the possibility of promoting grain growth in compact $Rb_3Sb_2I_9$ films by controlling the supersaturation level during annealing. We thus adopted a method, which we refer to as Reduced Supersaturation Annealing (RSA), that involves limiting the solvent evaporation rate during the annealing step. As shown in **Figure 1a**, a salient aspect of this method is that the hotplate annealing step is carried out with the as-spun $Rb_3Sb_2I_9$ films turned over onto a glass slide. Capping the substrate reduces the solvent evaporation rate, and, in turn, the supersaturation level in the $Rb_3Sb_2I_9$ film being formed. In contrast to classic vapor annealing,[14,47] RSA involves an extremely low (i.e., residual) amount of solvent, thus preventing the perovskite film from being significantly re-dissolved and altered. (See the Experimental Section and **Figure S3** for further details.)

Apart from the supersaturation level, the annealing temperature can also have a profound impact on the final morphology of a perovskite film. In this regard, it is noteworthy that a number of reports from the broader perovskite research landscape evidence that annealing temperatures > 200 – 250 °C may lead to films with particularly large grain size.[48,49] We found, however, that a straightforward annealing step at such high-temperatures is not practicable for $Rb_3Sb_2I_9$, as it leads to its decomposition (**Figure S4**). To the end of investigating the effect of high-temperature annealing without having the $Rb_3Sb_2I_9$ films undergo decomposition, we thus developed a modified high-temperature (> 200 °C) annealing scheme. This involves carrying out the annealing step while the sample is placed in a closed container saturated with SbI_3 vapor (see **Figure 1a**). In particular, the SbI_3 vapor source in this process consists of SbI_3 powder placed in the vicinity of the $Rb_3Sb_2I_9$ samples (see Experimental Section and **Figure S5** for details). The SbI_3 powder is in a dry form, as we found that the additional presence of any solvent vapors negatively impacts the reproducibility of the process. We refer to this process as High-Temperature Vapor Annealing (HTVA). HTVA processing of $Rb_3Sb_2I_9$ films is enabled by the comparatively low melting point of SbI_3 (170 °C at atmospheric pressure) and by its appreciable vapor pressure at temperatures in excess of 200 °C.[50,51] As a result, the SbI_3 in the gas phase prevents the loss of SbI_3 from the as-spun $Rb_3Sb_2I_9$ film even at temperatures in excess of 200 °C. Evidence of this mechanism is provided by Energy Dispersive X-Ray Spectroscopy (EDS) measurements, which indicate that $Rb_3Sb_2I_9$ films annealed at temperatures above 200 °C maintain their Sb/I ratio at the expected stoichiometric level (**Figure S6** and **Table S1**). This is in addition to the fact that high-temperature annealing in an atmosphere saturated with SbI_3 vapor also allows the films to preserve their overall substrate coverage and their crystallographic, electronic, and optical absorption properties (*vide infra*). Consequently, HTVA enables the

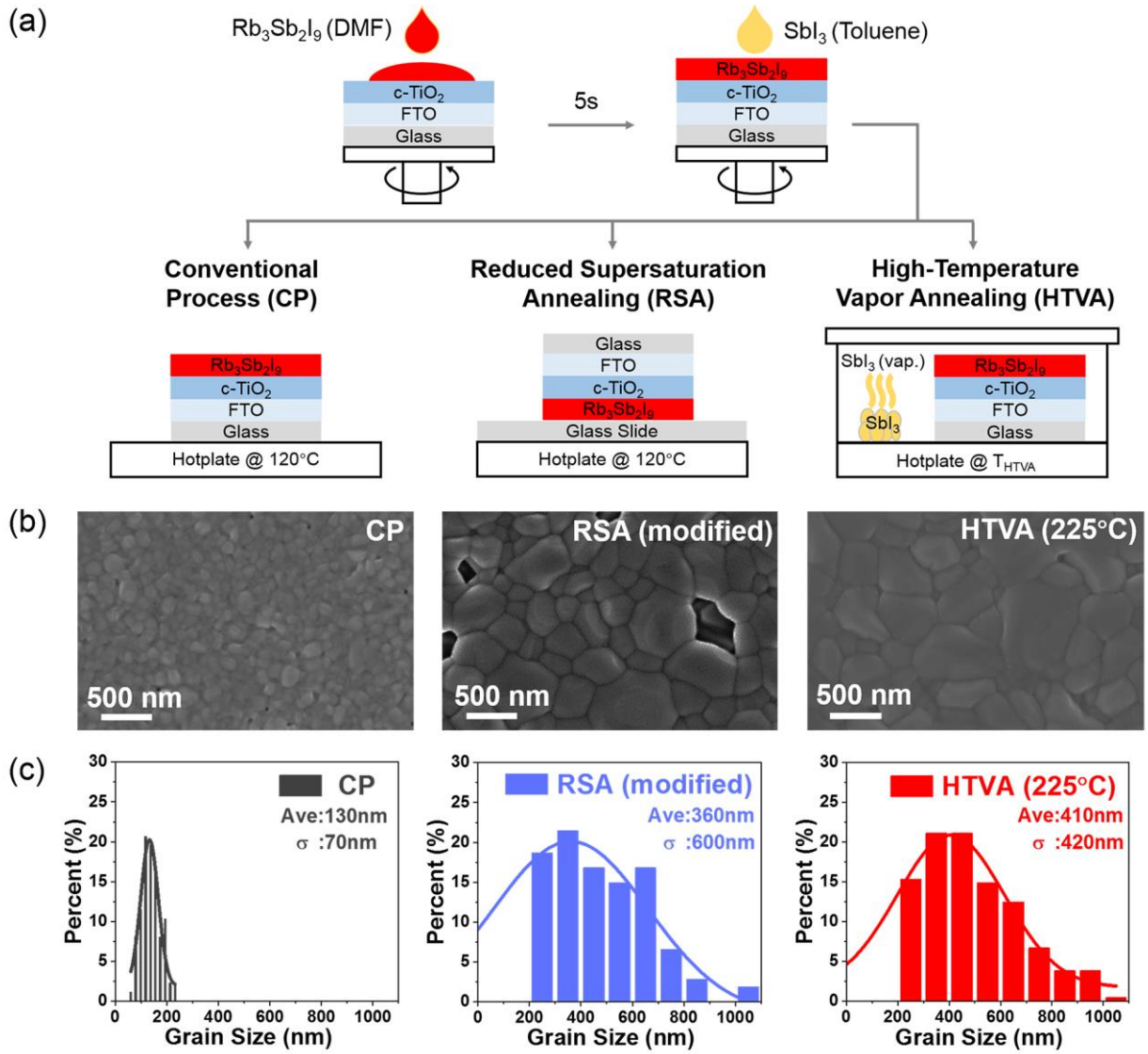

Figure 1 (a) Depiction of essential process steps in CP, RSA, and HTVA. (b) SEM images of the resulting films. (c) Corresponding (apparent) grain size distributions.

optimization of the annealing process at temperatures higher than it would be otherwise possible, which may potentially have a favorable impact on the film microstructure.

Figure 1b shows the scanning electron microscopy (SEM) images of $Rb_3Sb_2I_9$ films processed on planar substrates through the different deposition processes (CP, RSA, and HTVA) we have investigated. Unless otherwise noted, the planar substrates consist of TiO_2|FTO|glass (FTO: fluorine-doped tin-oxide). Our CP films present an average apparent grain size of 130 nm, as per SEM (**Figure 1b-c**), similar to earlier reports of CP films on mesoporous substrates.[36] In contrast, RSA films exhibit a dramatic improvement in apparent grain size, up to 1 µm in lateral dimensions (**Figure 1b-c**). This shows that grain growth in $Rb_3Sb_2I_9$ films deposited on a planar substrate can be controlled during the annealing step by reducing the solvent evaporation rate, which in turn determines the supersaturation level. Running the annealing step at the highest solvent evaporation rate possible (for a given annealing temperature), as in CP, enhances nucleation over grain growth, leading to small apparent grain size (**Figure S2**). On the contrary, curbing the evaporation rate shifts the balance towards grain growth (**Figure S2**), thus allowing the dramatic apparent grain size improvement observed in RSA samples. Further evidence of this mechanistic picture is provided by the fact that, while leading to particularly large apparent grain size, RSA in the basic form described so far also yields large pinholes (**Figure S3**). This denotes that grain growth in basic RSA runs at a particularly low supersaturation level (i.e., with a comparatively large amount of solvent), which determines a pronounced imbalance between the grain growth rate and the nucleation rate. Thus, we devised a modified RSA scheme, in which a straightforward pre-annealing step at the moderate temperature of 50 °C is conducted prior to RSA proper (see Experimental Section and **Figure S3** for details). This enables a controlled reduction of the residual amount of solvent in the sample prior to RSA, in turn allowing RSA to run at a slightly higher supersaturation level. Indeed, the modified RSA scheme successfully delivers films with apparent grain size of 360 nm on average and up to 1 µm, while achieving a significantly lower pinhole count (see **Figure 1b**). Interestingly, modified RSA

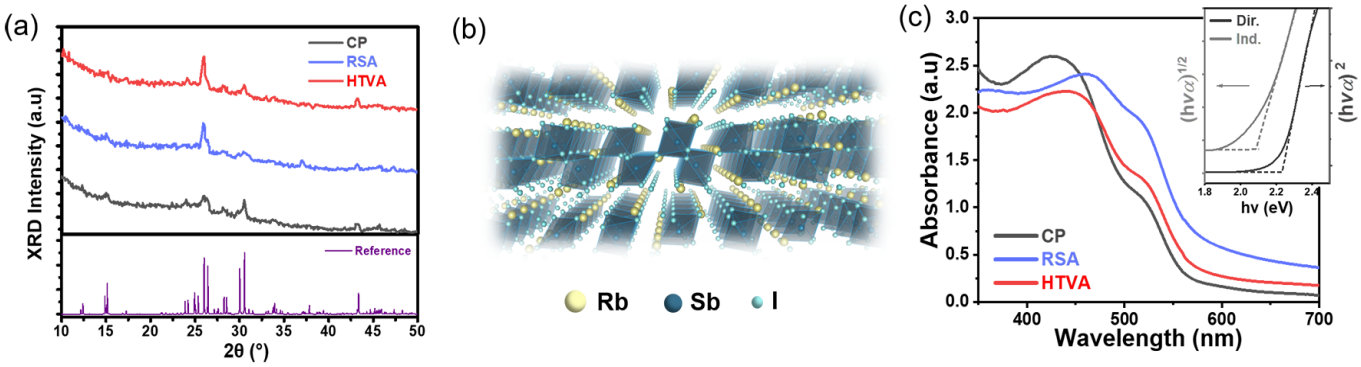

Figure 2 (a) XRD patterns of $Rb_3Sb_2I_9$ films processed via CP, RSA, and HTVA. The reference pattern[52] in also shown. (b) Schematic depiction of the two-dimensional $Rb_3Sb_2I_9$ structure. (c) Optical absorption spectra of $Rb_3Sb_2I_9$ films processed via CP, RSA, and HTVA. Inset: Tauc plots of a CP sample.

on planar FTO results in $Rb_3Sb_2I_9$ films that, while also presenting a maximum apparent grain size of 1 µm, manifest a significant lower pinhole count and pinhole size (**Figure S7**)—denoting a slight sensitivity of RSA to the details of the substrate surface.

HTVA also delivers a dramatic apparent grain size enhancement. When conducted at around 180 °C, the apparent grain size increases up to 400 nm (**Figure S8**) (average at ≈ 200 nm; compare with the average of 130 nm in CP films), while at temperatures approaching 225 °C it becomes as large as ≈ 1 µm (average at ≈ 410 nm) (**Figure 1b-c**). Considering that the SbI_3 vapor in HTVA serves as a means of preventing the loss of SbI_3 from the $Rb_3Sb_2I_9$ films, the domain growth attained with HTVA (**Figure 1b**) can be related to the kinetic enhancement resulting from the high temperature used in this process. Further, inspection of **Figure 1b** reveals that HTVA produces the same qualitative outcome as RSA. However, the quantitative comparison (**Figure 1c**) based on the apparent grain size distributions reveals that HTVA in fact leads to films with slightly larger apparent grain size. While it could be extrapolated that higher temperatures would lead to even bigger grains, however, we found that HTVA-processed $Rb_3Sb_2I_9$ films become optically transparent for annealing temperatures higher than 250 °C (**Figure S9**). This is likely due to the exhaustion of the SbI_3 source—due the complete evaporation of the initial amount of SbI_3 powder, which condenses and recrystallizes on the upper half of the container inner surface.

The X-ray diffraction (XRD) patterns of all $Rb_3Sb_2I_9$ film types (i.e., CP-, RSA-, and HTVA-processed) present peaks (**Figure 2a**) that conform to the 2D perovskite structure (**Figure 2b**) reported in the literature.[36] The grain size estimated using the Scherrer method[53] (assuming 0.9 as the value of the shape factor due to the cubic shape of the domains imaged via SEM,[54] and taking into account the instrumental broadening) is significantly smaller than the size of the grain-like domains observed from SEM. It is therefore clear that the grain-like domains imaged via SEM consist of several smaller crystallites. Owing to the high complexity of the diffraction pattern of $Rb_3Sb_2I_9$ (see reference pattern[52] in **Figure 2a**), each of the measured peaks in the XRD patterns is in fact composed of several diffraction peaks (see **Figure S10**). Therefore, we were not able to reliably obtain further details, such as the trend in the crystallite size. Nonetheless, these XRD measurements are insightful insofar as they reveal that the SEM-derived domains consist of several smaller crystallites.

Figure 2c illustrates the absorbance spectra of $Rb_3Sb_2I_9$ films (200 nm thick) deposited via CP, RSA, and HTVA, as derived from UV-visible spectrophotometry. The apparent in-band absorption coefficient of all films is in the region of $1{\cdot}10^5$ cm^{-1} (i.e., comparable to that of mainstream lead-halide perovskites) (see **Figure S11**). This indicates that 200 – 300 nm thick films can absorb > 90% of the in-band photons when embedded within a sandwich-type device structure. All films give an absorption onset of approximately 600 nm, which suggests potential for top-cells in tandem photovoltaics and indoor photovoltaics. For instance, in the Shockley-Queisser limit, a semiconductor with a bandgap such as $Rb_3Sb_2I_9$ could deliver a power conversion efficiency in the region of 30% in combination with crystalline silicon.[55,56] In the broader optoelectronics domain, the absorption properties of our $Rb_3Sb_2I_9$ films are suitable for green-blue photodetection.[57–59] Additionally, an absorption onset of around 600 nm indicates an excellent match with indoor light sources, therefore pointing to the significant potential of $Rb_3Sb_2I_9$ for indoor light harvesting.[24] The direct and indirect optical gap values extracted from the corresponding Tauc plots are 2.24 eV and 2.1 eV, respectively (inset of **Figure 2c**) (these values are independent from the adopted deposition process; see **Figure S11**). The two types of transition are particularly close in energy, consistently with the literature.[35,36] The ionization energy of CP $Rb_3Sb_2I_9$ films determined from Ultraviolet Photoelectron Spectroscopy (UPS) is at 5.56 eV with respect to vacuum, while the Fermi level lies at 4.41 eV (**Figure S12**). Similar values are obtained from HTVA and RSA films (**Figure S12**). Taking the minimum gap value inferred from the Tauc plots as a good approximation of the electronic gap of $Rb_3Sb_2I_9$ (in fact, excitonic effects would introduce only a minor correction), we thus estimate that the conduction band minimum is at 3.4 eV below the vacuum level. These key energy levels are in agreement with prior literature.[36] In particular, the Fermi level is close to midgap, which suggests that our $Rb_3Sb_2I_9$

Table 1 Performance parameters of $Rb_3Sb_2I_9$ devices (best and average, as per PCE) under AM1.5G illumination. Average and standard deviation values presented here were calculated from 40 devices of each sample

		V_{oc} (V)	J_{sc} (mA cm^{-2})	FF	PCE (%)
RSA	Best	0.56	5.50	0.36	1.12
	Average	0.56±0.03	3.40±0.59	0.42±0.05	0.79±0.08
HTVA	Best	0.61	5.54	0.40	1.35
	Average	0.58±0.03	4.99±0.28	0.39±0.02	1.11±0.11
CP	Best	0.50	1.72	0.45	0.38
	Average	0.49±0.03	1.39±0.19	0.46±0.04	0.32±0.05

films are potentially well-suited for integration into p-i-n/n-i-p sandwich-type devices.[60]

For the purpose of assessing their photoconversion potential, we integrated our $Rb_3Sb_2I_9$ films into devices featuring a planar device stack: FTO|c-TiO_2|$Rb_3Sb_2I_9$|Poly-TPD|Au (c-TiO_2, compact titania; poly-TPD, Poly(N,N'-bis-4-butylphenyl-N,N'-bisphenyl)benzidine) (**Figure 3a**). The specific choice of hole and electron transport layers follows from energetic considerations. As a standard means of evaluating their photoconversion capability, we characterized the current-voltage (J-V) characteristics of our CP, RSA, and HTVA devices under simulated solar illumination (AM1.5G). We stress that such measurements were carried out as they allow a direct comparison with prior relevant literature on $Rb_3Sb_2I_9$, while, in the optoelectronic domain, $Rb_3Sb_2I_9$ is most promising for top-cells in tandem photovoltaic, indoor photovoltaics, and blue-green photodetection. The corresponding current density-voltage characteristics are shown in **Figure 3b**, while key performance parameters are listed in **Table 1**. CP-deposited $Rb_3Sb_2I_9$ films deliver a short-circuit current density (J_{sc}) of 1.72 mA cm^{-2} and a PCE of 0.38%, which are lower than earlier reports utilizing the same (i.e., CP) deposition method but featuring a mesoporous device architecture (**Table 2**, Ref. 36,37).

This suggests that compact $Rb_3Sb_2I_9$ films with small grains inherently suffer from poor photovoltaic performance, hence they benefit from the mesoporous photogeneration/charge collection aid (in the form of mesoporous TiO_2) employed in all prior works (**Table 2**, Ref. 35,36,37). Devices comprising RSA and HTVA films deliver significantly higher PCE values, up to 1.11% and 1.35%, respectively—a more-than-threefold improvement on the CP case. This boost primarily results from a threefold rise in J_{sc} (5.50 mA cm^{-2} and 5.54 mA cm^{-2} in RSA and HTVA samples, respectively). It is noteworthy that in some instances HTVA devices deliver a J_{sc} as large as 6.35 mA cm^{-2} (**Figure S13**). Furthermore, while all methods deliver J-V characteristics under AM1.5G illumination with only minor hysteresis (**Figure S14**), the latter is in fact smallest in HTVA samples (see hysteresis index values in **Figure 3b**). Finally, the distribution of the key photovoltaic parameters of CP, HTVA, and RSA devices is provided in **Figure S15**.

These results enable a fresh assessment of the photoconversion and photovoltaic potential of $Rb_3Sb_2I_9$: films with improved microstructure (e.g., HTVA-processed) deliver not only state-of-the-art PCE, but also the highest J_{sc} of all $Rb_3Sb_2I_9$ devices under AM1.5G illumination reported to date (**Table 2**). Importantly, this is achieved while relying on the inherent charge

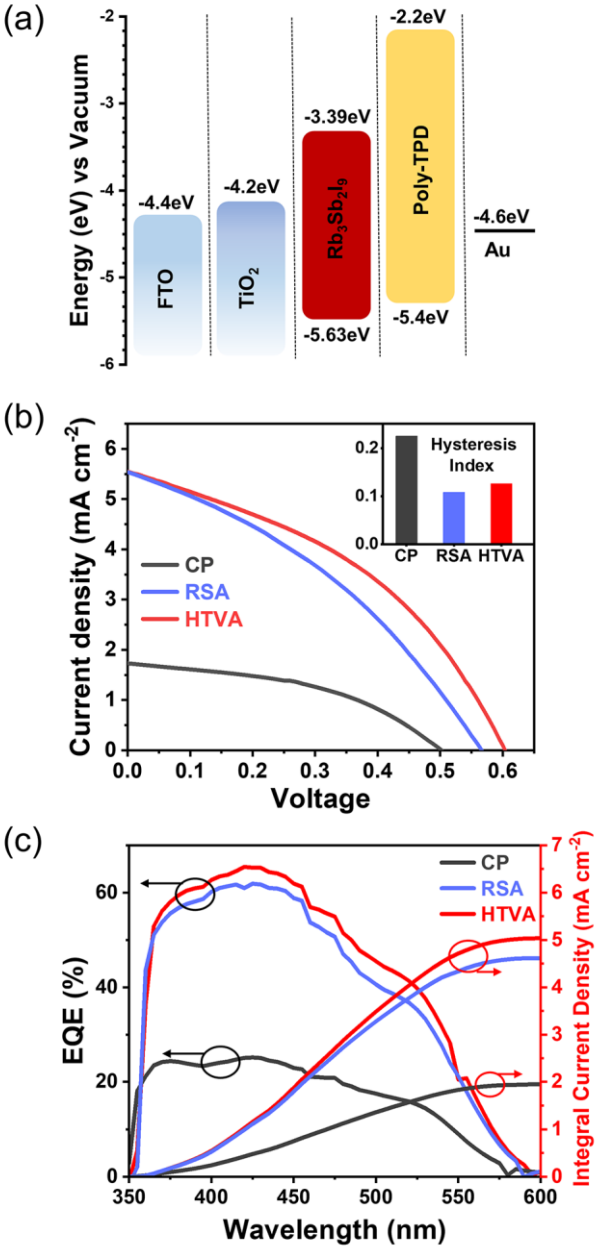

Figure 3 (a) Key energy levels of the layers employed in our $Rb_3Sb_2I_9$ devices. (b) Photocurrent-voltage characteristics of different types of $Rb_3Sb_2I_9$ devices under simulated AM1.5G illumination (inset: magnitude of the hysteresis index, calculated as ($PCE_{Reverse}$ - $PCE_{Forward}$)/$PCE_{Reverse}$; see Figure S14 for details). (c) Corresponding EQE spectra.

photogeneration and transport properties of $Rb_3Sb_2I_9$, i.e., without the use of a mesoporous TiO_2 layer serving as a photogeneration/collection aid—as explored in earlier reports (**Table 2**). To put this in context, the maximum possible theoretical photocurrent density[36] for a semiconductor with a bandgap of 2.24 eV (as $Rb_3Sb_2I_9$) is ~10 mA cm^{-2}. By reaching up to ~65 % of this theoretical limit (**Figure S13**), high-quality $Rb_3Sb_2I_9$ films enable a significant leap forward toward their optimum photocurrent performance. Additionally, the considerable photocurrent increase with respect to the prior state of the art (relying on a mesoporous architecture) indicate that efficient photogeneration in $Rb_3Sb_2I_9$ does not require a

Table 2 Photovoltaic performance parameters of $Rb_3Sb_2I_9$ devices from the literature.

Device Structure	V_{oc} (V)	J_{sc} (mA cm^{-2})	FF (%)	PCE (%)	EQE_{max} (%)	Ref
FTO|c-TiO_2|m-TiO_2| $Rb_3Sb_2I_9$|Spiro-OMeTAD/Au	0.66	1.84	63	0.76	No data	35
FTO|c-TiO_2|m-TiO_2| $Rb_3Sb_2I_9$|Poly-TPD|Au	0.55	2.11	57	0.66	28	36
FTO|c-TiO_2|m-TiO_2| $Rb_3Sb_2I_9$|Spiro-OMeTAD|Au	0.55	4.25	60	1.37	26	61
FTO|c-TiO_2|$Rb_3Sb_2I_9$| Poly-TPD/Au	0.61	5.54	40	1.35	65.4	This work

distributed interface with TiO_2, notwithstanding that the primary photoexcitations at the absorption edge in $Rb_3Sb_2I_9$ expectedly have an excitonic character.

An inner view of the photoconversion process in the three $Rb_3Sb_2I_9$ film types is offered by their external quantum efficiency (EQE) spectra (**Figure 3c**). All of them manifest an onset at around 600 nm and show good agreement with the absorption data. In particular, HTVA and RSA films deliver a maximum EQE of 65.4% and 61.9%, ≈ 2.5 times higher than that of CP films (maximum EQE of 25.2%). In fact, to the best of our knowledge, HTVA $Rb_3Sb_2I_9$ films achieve the highest EQE reported to date not only for Sb-halide perovskite derivatives, but also for all electronically and structurally akin Bi-halide perovskite derivatives—i.e., for all compounds with formula $A_3M_2X_9$, A^+: organic/inorganic cation, M: Sb^{3+}/Bi^{3+}, and X^-: halide anion (**Table 2** and **Table S2**). As a consistency check, the calculated current densities under AM1.5G illumination derived from the EQE spectra of HTVA and RSA films (**Figure 3c**) amount to 5.05 mA cm^{-2} and 4.64 mA cm^{-2}, respectively, showing a close match with the experimental J_{sc} values (≈ 5.5 mA cm^{-2}).

The remarkable boost in photoconversion efficiency is obviously associated with the improved film quality of HTVA- and RSA-processed $Rb_3Sb_2I_9$ over the CP-processed counterpart. In fact, the observed PCE/EQE trend qualitatively reflects the same trend in grain size. Notwithstanding the obvious role of microstructure, the photoconversion efficiency is in fact a direct manifestation of the capability of photogenerated charges to reach the respective electrodes prior to recombination. Microscopic insight into the observed performance boost can thus be gained by ascertaining the impact of the microstructure on the microscopic optoelectronic properties such as recombination and charge transport. Photocurrent-optical power ($I_{ph} - P_{opt}$) characteristics—which we measured on HTVA and CP devices under pulsed illumination (**Figure 4a**)—provide valuable insight into the recombination behavior of different types of $Rb_3Sb_2I_9$ films. (In view of the similar photoconversion efficiencies of HTVA- and RSA-processed $Rb_3Sb_2I_9$, in the following we shall only refer to the former when discussing high-quality films and corresponding devices.) These characteristics conform to a linear trend at low and at high optical power densities (up to levels comparable to AM1.5G illumination), while at intermediate power values a sublinear trend emerges. Within the classic framework originally developed by A. Rose[62] and further elaborated upon by R. H. Bube,[63] the observed behavior is consistent with one-center recombination through defect states of the same class (i.e., with similar electron and hole capture cross-

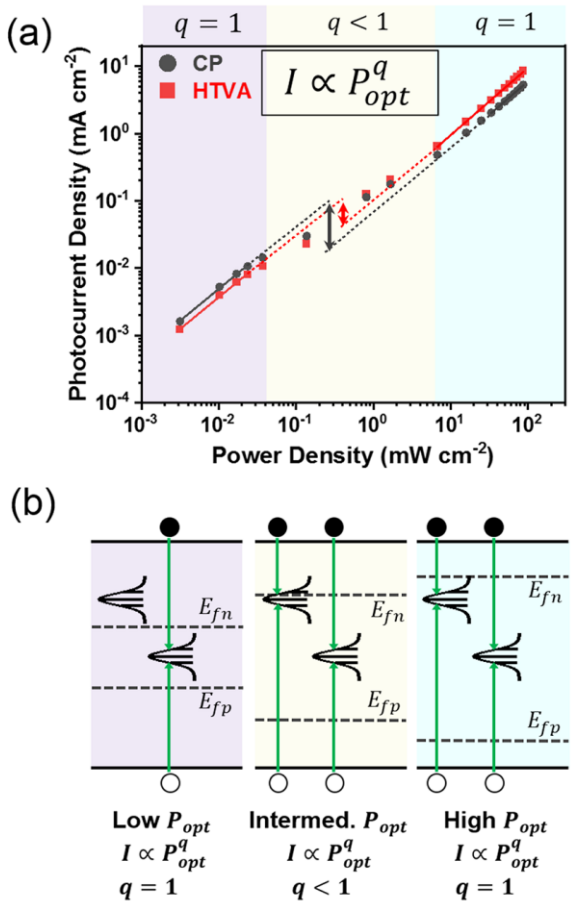

Figure 4 (a) Photocurrent-optical power ($I_{ph} - P_{opt}$) characterization under pulsed illumination at λ = 505 nm and in short-circuit conditions acquired from CP and HTVA devices. (b) Schematic depiction of the one-center model rationalizing the observed $I_{ph} - P_{opt}$ dependence.

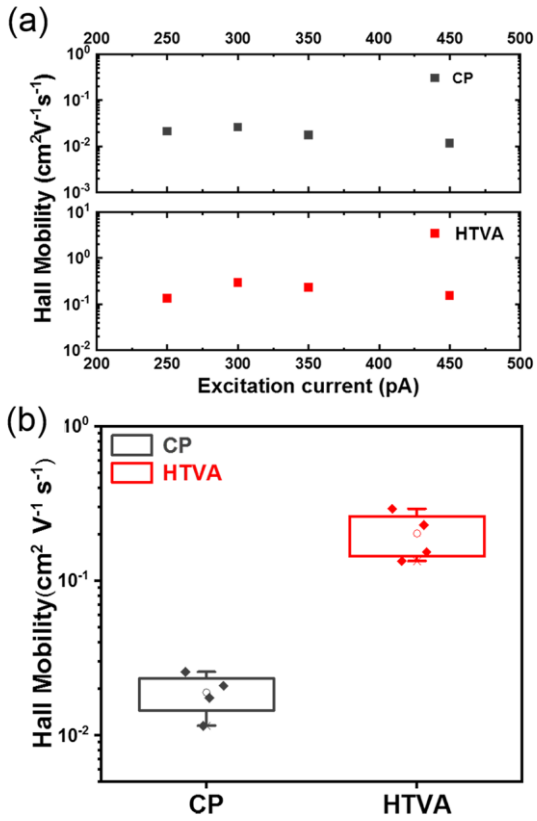

Figure 5 Hall mobility values in CP and HTVA films.(a) with respect to the excitation current;(b) distribution

sections) yet located at different energies in the forbidden gap (**Figure 4b**) (e.g., see sections 2.2.6 and 2.2.8 of Ref. 62 and pp. 336-337 and Figure. 11.3-1a of Ref. 63). This is not to be confused with the two-center model also reported by the same authors, which involves defect states of significantly different capture cross-sections and corresponds to a *superlinear* photocurrent-power dependence ($I_{ph} \propto P_{opt}^{q}$, $q > 1$)—hence, having no relationship with our experimentally observed trend. Consistently with the one-center model, in our system at low optical power only some of the defect states (i.e., approximately the ones embraced within the electron and hole quasi-Fermi levels) act as recombination centers. Therefore, a constant photosensitivity ensues ($I_{ph} \propto P_{opt}^{q}$, $q = 1$) (**Figure 4a-b**). As the optical power increases, the quasi-Fermi levels move closer to the band edges, eventually embracing further defect states, which turn into additional recombination centers. The resulting increase in the number of recombination centers causes the photosensitivity to drop with optical power, i.e., $I_{ph} \propto P_{opt}^{q}$ with $q < 1$ (*sublinear region*) (**Figure 4a-b**). Finally, at sufficiently high power, all defect states fall within the quasi-Fermi levels, hence the photosensitivity is again a constant, i.e., $I_{ph} \propto P_{opt}^{q}$ with $q = 1$ (**Figure 4a-b**). In view of the consistency of this model with our findings, the photosensitivity reduction in the sublinear region (see arrows in $I_{ph} - P_{opt}$ plot, **Figure 4a**) expectedly relates to the number of corresponding defect states that turn into recombination centers. Additionally, we infer that these states are located around the same energy within the forbidden gap in both HTVA and CP films, considering that the sublinear region in both occurs over the same P_{opt} values (**Figure 4a**). As the photosensitivity reduction is more pronounced in the CP case (**Figure 4a**), we thus conclude that HTVA samples present a significantly smaller concentration of such recombination centers.

The photoconversion efficiency of $Rb_3Sb_2I_9$ also relates to its charge transport capabilities. We thus investigated the carrier mobility of our $Rb_3Sb_2I_9$ films via Hall effect characterization (**Figure 5**). We conducted this investigation on samples with van der Pauw structure, incorporating the same $Rb_3Sb_2I_9$ films that we employed in our sandwich-type devices discussed earlier. In view of the large resistivity we experimentally measured from the van der Pauw samples, we specifically resorted to a Hall effect characterization methodology that involves applying a sinusoidally modulated (AC) magnetic field and concurrently sensing the Hall voltage via a lock-in amplifier. This has been known in the specialized Hall effect literature to overcome the challenges associated with the Hall effect characterization of high-resistivity samples, which can lead to measurement artifacts due to geometric non-idealities and thermoelectric effects.[64] In fact, AC-magnetic-field Hall effect characterization has been successful in characterizing semiconductors with Hall mobility values well below 1 $cm^2\ V^{-1}\ s^{-1}$.[64–66] AC-magnetic-field Hall characterization was conducted on our samples under a magnetic field of 0.42 T modulated at 100 mHz. The near-invariance of the extracted Hall mobility with respect to the excitation current indicates that such samples conform to the basic Hall effect model (**Figure 5a**). In particular, from such measurements we obtained that HTVA films give an average Hall mobility of 0.26 $cm^2\ V^{-1}\ s^{-1}$, while in CP films this amounts to 0.04 $cm^2\ V^{-1}\ s^{-1}$. The large mobility difference between CP and HTVA films can be attributed to their different microstructure. Indeed, CP films consist of domains with average lateral size approximately equal to 130 nm, while the same dimension is of the order of 400 nm in HTVA films. Therefore, CP films have a higher density of domain boundaries. As domain boundaries are expected to pose a limitation on charge transport, the significantly lower density of domain boundaries in HTVA films is consistent with its much higher experimental charge carrier mobility.

Our experimental photocurrent-power characteristics and Hall effect measurements jointly allow us to qualitatively explain the performance improvement attained with our high-quality $Rb_3Sb_2I_9$ films. Indeed, we have found that HTVA films feature a smaller density of deep levels and larger carrier mobility. In turn, the photoconversion efficiency is expected to improve with carrier mobility and with a reduction in deep level concentration. Indeed, the photocurrent scales with the mobility-lifetime product $\mu\tau$ (e.g., $J_{ph} \propto \mu\tau$ according to a basic model formulation[67–69]). At a quantitative level, the specific EQE/photocurrent figures may result from the convolution of effects such as: the specifics of the carrier photocurrent-voltage dependence beyond the basic model $J_{ph} \propto \mu\tau$; the dependence of carrier mobility and lifetime on crystalline orientation and on optical power; electric field non-uniformities in the photoactive layer; difference in optical losses in the films. Overall, however, our findings are consistent with the fact that the microstructural improvement in our HTVA films has a favorable impact on their charge transport and photoconversion efficiency.

Conclusion

Our study presents strategies that improve the thin-film microstructure of $Rb_3Sb_2I_9$—an emerging lead-free perovskite derivative—and evaluates the impact of such improvement in terms of optoelectronic properties and device behavior. To the end of enhancing the film quality, we develop deposition strategies based on the control of the supersaturation level and on the high-temperature annealing in excess precursor vapor. These strategies enable an appreciable increase in the apparent grain size of compact $Rb_3Sb_2I_9$ films. Embedded into sandwich-type devices with a planar architecture, these films demonstrate high photoconversion efficiency. For instance, they deliver a peak EQE of 65.4%, the highest reported to date for antimony-halide perovskite derivatives and bismuth-halide homologs (i.e., compounds with formula $A_3M_2X_9$, A^+: organic/inorganic cation, M: Sb^{3+}/Bi^{3+}, and X^-: halide anion). Additionally, such high-quality films give a short-circuit photocurrent under AM1.5G illumination up to within 35% of the radiative limit. The merit of such performance improvement resulting from our high-quality $Rb_3Sb_2I_9$ films are particularly evident if one considers that they have been attained with a planar device architecture—i.e., doing without a mesoporous transport layer to aid charge extraction, as generally adopted with lead-free antimony-/bismuth-based perovskite derivatives in view of their alleged charge extraction limitations. In perspective, our findings show that $Rb_3Sb_2I_9$ has approached photoconversion efficiency figures that motivate the exploration of this material for use in top-cells for tandem photovoltaics, indoor photovoltaics, and photodetection.

Building on the observed performance improvement, we also present an optoelectronic characterization so as to provide insight into the capabilities and potential of our high-quality $Rb_3Sb_2I_9$ films. Hall effect and photocurrent-power characteristics allow us to establish that the microstructural improvement leads to a considerable increase in charge carrier mobility and a reduction in the number of recombination centers, thus rationalizing the associated photovoltaic performance boost. Therefore, it can be envisaged that the processing strategies we have developed for the microstructural and optoelectronic improvement of $Rb_3Sb_2I_9$ could be also pursued with other emerging antimony-/bismuth-based perovskite derivatives, potentially leading to the enhancement of their optoelectronic properties and device performance.

By demonstrating a considerable improvement in microstructure and photoconversion efficiency of $Rb_3Sb_2I_9$ in compact thin-film form, and by providing fresh insight into its photoconversion and photovoltaic properties, this work constitutes an important step for the advancement of lead-free antimony-halide perovskite derivatives and related compounds for photovoltaic and optoelectronic applications.

Experimental Section

***Materials*.** RbI (99.99%, Sigma-Aldrich), SbI_3 (99.999%, Alfa Aesar), dimethylformamide (DMF) (99.8%, J&K), toluene (99.5%, Yonghua Chemistry), Titanium(IV) Isopropoxide (97%, Sigma-Aldrich), [N,N'-bis(4-butylphenyl)-N,N'-bisphenylbenzidine] (poly-TPD) (M_W=6000~20000, Lumtec), chlorobenzene (99.8%, J&K).

***Perovskite Film Deposition*.** All steps of the perovskite film deposition (including solution preparation and annealing) were carried out in an N_2 filled glove box. 79.6 mg of RbI powder and 125.6 mg of SbI_3 powder (3:2 molar ratio) were dissolved in 0.5 mL of DMF (target solution concentration of 0.25 M). The solution was heated at 75 °C for more than 2 h and subsequently filtered (PTFE filter, pore size 0.22 μm). In regard to CP and HTVA samples, the solution was deposited as reported by Harikesh et al.[36] In regard to RSA samples, the solution was spin coated as reported by Harikesh et al.[36] except for the final toluene washing step, which was performed after annealing the samples at 120 °C. In particular, after depositing the perovskite films, HTVA samples were treated as follows: four substrates ($13.3 \cdot 15.3 mm^2$) were placed in a closed glass container (250 mL in volume) together with 50 mg of SbI_3 powder; the container was placed on a hotplate at 225 °C for 10 min; the temperature was then lowered to 150 °C and maintained at this level for 10 min; finally, the substrates were taken out of the container and allowed to cool down. In particular, after depositing the perovskite films, RSA samples were treated as follows: a substrate coated with an as-deposited film (without washing with toluene) was placed on a hotplate at 50 °C for 1 min; the substrate was then turned over onto a clean glass substrate placed on a hotplate at 120 °C (10 min); the substrate was then spun at 4000 rpm for 30 s while dispensing 100 μL of toluene so as to remove excess SbI_3; the substrate was finally annealed at 120 °C for 10 min.

***Thin Film Characterization*.** Scanning electron microscope (SEM) images were acquired with a ZEISS SUPRA 55 field-emission electron microscope under high vacuum (electron energy = 5 keV). X-ray diffraction (XRD) spectra were measured with an Empyrean X-ray diffractometer with monochromatic 4 Cu Kα irradiation (wavelength = 1.5406 Å). UV-Vis absorption spectra were measured with a PerkinElmer UV-Vis spectrophotometer. UPS spectra were acquired with a Kratos Analytical Himadzu X-ray photoelectron spectrometer. Energy-dispersive X-ray spectroscopy (EDS) were acquired with a ZEISS SUPRA 55 field-emission electron microscope under high vacuum (electron energy = 15 keV).

Device Fabrication. Glass substrates with pre-patterned fluorine-doped tin oxide (FTO) electrodes (Liaoning Youxuan New Energy Technology Co.) were cleaned in an ultrasonic bath with deionized water, acetone, and ethyl alcohol (10 min each). After drying with N_2 gas, they were treated with O_2 plasma (15 min). The substrates were then coated with a compact TiO_2 layer: the precursor solution was prepared (in an N_2 filled glove box) according to a procedure reported in the literature; [70] the solution (40 μL per substrate) was spin coated at 4000 rpm for 30 s (in an N_2 filled glove box); samples were then annealed at 450 °C for 40 min (in air). Subsequently, perovskite films were deposited according to the procedures detailed earlier. 10 mg of Poly-TPD powder was dissolved in 1 mL chlorobenzene; the solution (40 μL per substrate) was then spin coated on the perovskite layer at 4000 rpm for 30 s (in an N_2 filled glove box). Finally, 40 nm-thick gold electrodes were thermally evaporated

through a shadow masking to define an active area of 0.0725 cm^2.

Device and Optoelectronic Characterization. Current density-voltage (J-V), PCE, and EQE measurements were measured with a source-meter unit (Keithley 2400). The illumination source for EQE measurements was a monochromated broadband light source (Zolix Omni-λ200i), while PCE measurements relied on a simulated AM 1.5G source (100 mW/cm^2, Xenon lamp, Newport). The Hall-effect characterization was conducted with an electromagnet-based system (Lakeshore 8404) at room temperature, in air, and in the dark. Samples in the van der Pauw configuration were subjected to an AC magnetic field of 0.42 T (modulated at 100 mHz) and an excitation current in the 100 – 500 pA range. Transient photocurrent measurements were conducted with an LED source (OSRAM LV CK7P), the device photocurrent being acquired with a current amplifier (DHPCA-100) and an oscilloscope (Pico5444B).

Conflicts of interest

There are no conflicts to declare.

Acknowledgements

Fengzhu Li and Vincenzo Pecunia contributed equally to this work. The authors acknowledge financial support from the National Natural Science Foundation of China (61950410759, 61750110517 and 61805166) and the Jiangsu Province Natural Science Foundation (BK20170345). Additionally, this work is supported by the Collaborative Innovation Center of Suzhou Nano Science & Technology, the Priority Academic Program Development of Jiangsu Higher Education Institutions (PAPD), the 111 Project, and the Joint International Research Laboratory of Carbon-Based Functional Materials and Devices.

References

1 Q. Jiang, Y. Zhao, X. Zhang, X. Yang, Y. Chen, Z. Chu, Q. Ye, X. Li, Z. Yin and J. You, *Nat. Photonics*, 2019, **13**, 460–466.

2 M. Kim, G.-H. Kim, T. K. Lee, I. W. Choi, H. W. Choi, Y. Jo, Y. J. Yoon, J. W. Kim, J. Lee, D. Huh, H. Lee, S. K. Kwak, J. Y. Kim and D. S. Kim, *Joule*, 2019, **3**, 2179–2192.

3 K. L. Wang, R. Wang, Z. K. Wang, M. Li, Y. Zhang, H. Ma, L. S. Liao and Y. Yang, *Nano Lett*, 2019, **19**, 5176–5184.

4 Z. Xiao, R. A. Kerner, L. Zhao, N. L. Tran, K. M. Lee, T.-W. Koh, G. D. Scholes and B. P. Rand, *Nat. Photonics*, 2017, **11**, 108–115.

5 K. Lin, J. Xing, L. N. Quan, F. P. G. de Arquer, X. Gong, J. Lu, L. Xie, W. Zhao, D. Zhang, C. Yan, W. Li, X. Liu, Y. Lu, J. Kirman, E. H. Sargent, Q. Xiong and Z. Wei, *Nature*, 2018, **562**, 245–248.

6 L. Dou, Y. (Micheal) Yang, J. You, Z. Hong, W.-H. Chang, G. Li and Y. Yang, *Nat. Commun.*, 2014, **5**, 5404.

7 P. Ramasamy, D.-H. Lim, B. Kim, S.-H. Lee, M.-S. Lee and J.-S. Lee, *Chem. Commun.*, 2016, **52**, 2067–2070.

8 M. L. Petrus, J. Schlipf, C. Li, T. P. Gujar, N. Giesbrecht, P. Müller-Buschbaum, M. Thelakkat, T. Bein, S. Hüttner and P. Docampo, *Adv. Energy Mater.*, 2017, **7**, 1700264.

9 J. W. Xiao, L. Liu, D. Zhang, N. De Marco, J. W. Lee, O. Lin, Q. Chen and Y. Yang, *Adv. Energy Mater.*, 2017.

10 S. D. Stranks, G. E. Eperon, G. Grancini, C. Menelaou, M. J. Alcocer, T. Leijtens, L. M. Herz, A. Petrozza and H. J. Snaith, *Science (80-.).*, 2013, **342**, 341–344.

11 NREL, *Best Res. Effic. Chart*, 2019, https://www.nrel.gov/pv/cell-efficiency.html.

12 K. M. Boopathi, M. Ramesh, P. Perumal, Y.-C. Huang, C.-S. Tsao, Y.-F. Chen, C.-H. Lee and C.-W. Chu, *J. Mater. Chem. A*, 2015, **3**, 9257–9263.

13 Z. Xiao, C. Bi, Y. Shao, Q. Dong, Q. Wang, Y. Yuan, C. Wang, Y. Gao and J. Huang, *Energy Environ. Sci.*, 2014, **7**, 2619–2623.

14 Q. Chen, H. Zhou, Z. Hong, S. Luo, H. S. Duan, H. H. Wang, Y. Liu, G. Li and Y. Yang, *J Am Chem Soc*, 2014, **136**, 622–625.

15 A. K. Jena, A. Kulkarni and T. Miyasaka, *Chem Rev*, 2019, **119**, 3036–3103.

16 F. Igbari, Z. Wang and L. Liao, *Adv. Energy Mater.*, 2019, **9**, 1803150.

17 M. Lyu, J.-H. Yun, P. Chen, M. Hao and L. Wang, *Adv. Energy Mater.*, 2017, **7**, 1602512.

18 R. E. Brandt, J. R. Poindexter, P. Gorai, R. C. Kurchin, R. L. Z. Hoye, L. Nienhaus, M. W. B. Wilson, J. A. Polizzotti, R. Sereika, R. Žaltauskas, L. C. Lee, J. L. MacManus-Driscoll, M. Bawendi, V. Stevanović and T. Buonassisi, *Chem. Mater.*, 2017, **29**, 4667–4674.

19 L. C. Lee, T. N. Huq, J. L. MacManus-Driscoll and R. L. Z. Hoye, *APL Mater.*, 2018, **6**, 084502.

20 V. Andrei, R. L. Z. Hoye, M. Crespo-Quesada, M. Bajada, S. Ahmad, M. De Volder, R. Friend and E. Reisner, *Adv. Energy Mater.*, 2018, **8**, 1801403.

21 G. E. Eperon, T. Leijtens, K. A. Bush, R. Prasanna, T. Green, J. T.-W. Wang, D. P. McMeekin, G. Volonakis, R. L. Milot, R. May, A. Palmstrom, D. J. Slotcavage, R. A. Belisle, J. B. Patel, E. S. Parrott, R. J. Sutton, W. Ma, F. Moghadam, B. Conings, A. Babayigit, H.-G. Boyen, S. Bent, F. Giustino, L. M. Herz, M. B. Johnston, M. D. McGehee and H. J. Snaith, *Science (80-.).*, 2016, **354**, 861–865.

22 T. Krishnamoorthy, H. Ding, C. Yan, W. L. Leong, T. Baikie, Z. Zhang, M. Sherburne, S. Li, M. Asta, N. Mathews and S. G. Mhaisalkar, *J. Mater. Chem. A*, 2015, **3**, 23829–23832.

23 T. Miyasaka, A. Kulkarni, G. M. Kim, S. Öz and A. K. Jena, *Adv. Energy Mater.*, 2019, 1902500.

24 I. Mathews, S. N. Kantareddy, T. Buonassisi and I. M. Peters, *Joule*, 2019, **3**, 1415–1426.

25 V. Andrei, B. Reuillard and E. Reisner, *Nat. Mater.*, 2019, 1–6.

26 V. Pecunia, Y. Yuan, J. Zhao, K. Xia, S. Duhm, L. Portilla and F. Li, *Nano-Micro Lett.*

27 R. E. Brandt, V. Stevanović, D. S. Ginley and T. Buonassisi, *MRS Commun.*, 2015, **5**, 265–275.

28 K. M. McCall, C. C. Stoumpos, S. S. Kostina, M. G. Kanatzidis and B. W. Wessels, *Chem. Mater.*, 2017, **29**, 4129–4145.

29 A. J. Lehner, D. H. Fabini, H. A. Evans, C. A. Hébert, S. R. Smock, J. Hu, H. Wang, J. W. Zwanziger, M. L. Chabinyc and R. Seshadri, *Chem. Mater.*, 2015, **27**, 7137–7148.

30 H. Hu, B. Dong and W. Zhang, *J. Mater. Chem. A*, 2017, **5**, 11436–11449.

31 K. Yamada, H. Sera, S. Sawada, H. Tada, T. Okuda and H. Tanaka, *J. Solid State Chem.*, 1997, **134**, 319–325.

32 B. Saparov, F. Hong, J.-P. Sun, H.-S. Duan, W. Meng, S. Cameron, I. G. Hill, Y. Yan and D. B. Mitzi, *Chem. Mater.*, 2015, **27**, 5622–5632.

33 A. Singh, K. M. Boopathi, A. Mohapatra, Y. F. Chen, G. Li and C. W. Chu, *ACS Appl Mater Interfaces*, 2018, **10**, 2566–2573.

34 F. Umar, J. Zhang, Z. Jin, I. Muhammad, X. Yang, H. Deng, K. Jahangeer, Q. Hu, H. Song and J. Tang, *Adv. Opt. Mater.*, 2019, **7**, 1801368.

35 J.-P. Correa-Baena, L. Nienhaus, R. C. Kurchin, S. S. Shin, S. Wieghold, N. T. Putri Hartono, M. Layurova, N. D. Klein, J. R. Poindexter, A. Polizzotti, S. Sun, M. G. Bawendi and T. Buonassisi, *Chem. Mater.*, 2018, **30**, 3734–3742.

36 P. C. Harikesh, H. K. Mulmudi, B. Ghosh, T. W. Goh, Y. T. Teng, K. Thirumal, M. Lockrey, K. Weber, T. M. Koh, S. Z. Li, S. Mhaisalkar and N. Mathews, *Chem. Mater.*, 2016, **28**, 7496–7504.

37 S. Weber, T. Rath, K. Fellner, R. Fischer, R. Resel, B. Kunert, T. Dimopoulos, A. Steinegger and G. Trimmel, *ACS Appl. Energy Mater.*, 2019, **2**, 539–547.

38 A. K. Jena, A. Kulkarni and T. Miyasaka, *Chem. Rev.*, 2019, **119**, 3036–3103.

39 A. J. Pearson, G. E. Eperon, P. E. Hopkinson, S. N. Habisreutinger, J. T.-W. Wang, H. J. Snaith and N. C. Greenham, *Adv. Energy Mater.*, 2016, **6**, 1600014.

40 J. Xue, R. Wang, K. L. Wang, Z. K. Wang, I. Yavuz, Y. Wang, Y. Yang, X. Gao, T. Huang, S. Nuryyeva, J. W. Lee, Y. Duan, L. S. Liao, R. Kaner and Y. Yang, *J Am Chem Soc*, 2019, **141**, 13948–13953.

41 G. Jang, H. Kwon, S. Ma, S. Yun, H. Yang and J. Moon, *Adv. Energy Mater.*, 2019, **9**, 1901719.

42 B. Ghosh, B. Wu, X. Guo, P. C. Harikesh, R. A. John, T. Baikie, Arramel, A. T. S. Wee, C. Guet, T. C. Sum, S. Mhaisalkar and N. Mathews, *Adv. Energy Mater.*, 2018, **8**, 1802051.

43 S. P. Senanayak, B. Yang, T. H. Thomas, N. Giesbrecht, W. Huang, E. Gann, B. Nair, K. Goedel, S. Guha, X. Moya, C. R. McNeill, P. Docampo, A. Sadhanala, R. H. Friend and H. Sirringhaus, *Sci. Adv.*, 2017, **3**, e1601935.

44 O. G. Reid, M. Yang, N. Kopidakis, K. Zhu and G. Rumbles, *ACS Energy Lett.*, 2016, **1**, 561–565.

45 Z. Chu, M. Yang, P. Schulz, D. Wu, X. Ma, E. Seifert, L. Sun, X. Li, K. Zhu and K. Lai, *Nat. Commun.*, 2017, **8**, 2230.

46 H. Li, G. Wu, W. Li, Y. Zhang, Z. Liu, D. Wang and S. Liu, *Adv. Sci.*, 2019, 1901241.

47 Z. Xiao, Q. Dong, C. Bi, Y. Shao, Y. Yuan and J. Huang, *Adv. Mater.*, 2014, **26**, 6503–6509.

48 M. Khazaee, K. Sardashti, J.-P. Sun, H. Zhou, C. Clegg, I. G. Hill, J. L. Jones, D. C. Lupascu and D. B. Mitzi, *Chem. Mater.*, 2018, **30**, 3538–3544.

49 W. Ning, F. Wang, B. Wu, J. Lu, Z. Yan, X. Liu, Y. Tao, J. M. Liu, W. Huang, M. Fahlman, L. Hultman, T. C. Sum and F. Gao, *Adv Mater*, 2018, **30**, e1706246.

50 R. Kreizman, A. N. Enyashin, F. L. Deepak, A. Albu-Yaron, R. Popovitz-Biro, G. Seifert and R. Tenne, *Adv. Funct. Mater.*, 2010, **20**, 2459–2468.

51 N. W. Gregory, *J. Chem. Eng. Data*, 1996, **41**, 107–112.

52 J.-H. Chang, T. Doert and M. Ruck, *Zeitschrift für Anorg. und Allg. Chemie*, 2016, **642**, 736–748.

53 B. E. Warren, *X-ray Diffraction*, Courier Corporation, 1990.

54 J. I. Langford and A. J. C. Wilson, *J. Appl. Crystallogr.*, 1978, **11**, 102–113.

55 J.-C. Hebig, I. Kühn, J. Flohre and T. Kirchartz, *ACS Energy Lett.*, 2016, **1**, 309–314.

56 W. Shockley and H. J. Queisser, *J. Appl. Phys.*, 1961, **32**, 510–519.

57 C. Li, C. Han, Y. Zhang, Z. Zang, M. Wang, X. Tang and J. Du, *Sol. Energy Mater. Sol. Cells*, 2017, **172**, 341–346.

58 M. Shoaib, X. Zhang, X. Wang, H. Zhou, T. Xu, X. Wang, X. Hu, H. Liu, X. Fan, W. Zheng, T. Yang, S. Yang, Q. Zhang, X. Zhu, L. Sun and A. Pan, *J. Am. Chem. Soc.*, 2017, **139**, 15592–15595.

59 V. Pecunia, *J. Phys. Mater.*, 2019, **2**, 042001.

60 W.-J. Yin, J.-H. Yang, J. Kang, Y. Yan and S.-H. Wei, *J. Mater. Chem. A*, 2015, **3**, 8926–8942.

61 S. Weber, T. Rath, K. Fellner, R. Fischer, R. Resel, B. Kunert, T. Dimopoulos, A. Steinegger and G. Trimmel, *ACS Appl. Energy Mater.*, 2018, **2**, 539–547.

62 A. Rose, *RCA Rev.*, 1951, **12**, 362–414.

63 R. H. Bube, *Photoconductivity of Solids*, John Wiley & Sons, Inc., New York, NY, USA, 1960.

64 J. Lindemuth and S.-I. Mizuta, in *Proc. SPIE 8110, Thin Film Solar Technology III*, SPIE, 2011, p. 81100I.

65 D. T. Scholes, P. Y. Yee, J. R. Lindemuth, H. Kang, J. Onorato, R. Ghosh, C. K. Luscombe, F. C. Spano, S. H. Tolbert and B. J. Schwartz, *Adv. Funct. Mater.*, 2017, **27**, 1702654.

66 A. J. E. Rettie, H. C. Lee, L. G. Marshall, J.-F. Lin, C. Capan, J. Lindemuth, J. S. McCloy, J. Zhou, A. J. Bard and C. B. Mullins, *J. Am. Chem. Soc.*, 2013, **135**, 11389–11396.

67 H. Azimi, T. Ameri, H. Zhang, Y. Hou, C. O. R. Quiroz, J. Min, M. Hu, Z.-G. Zhang, T. Przybilla, G. J. Matt, E. Spiecker, Y. Li and C. J. Brabec, *Adv. Energy Mater.*, 2015, **5**, 1401692.

68 R. S. Crandall, *J. Appl. Phys.*, 1982, **53**, 3350–3352.

69 T. Kirchartz, T. Agostinelli, M. Campoy-Quiles, W. Gong and J. Nelson, *J. Phys. Chem. Lett.*, 2012, **3**, 3470–3475.

70 M. Saliba, T. Matsui, J. Y. Seo, K. Domanski, J. P. Correa-Baena, M. K. Nazeeruddin, S. M. Zakeeruddin, W. Tress, A. Abate, A. Hagfeldt and M. Grätzel, *Energy Environ. Sci.*, 2016, **9**, 1989–1997.

Supporting Information for

Microstructural and Photoconversion Efficiency Enhancement of Compact Films of Lead-Free Perovskite Derivative $Rb_3Sb_2I_9$†

Fengzhu Li,[‡a] Yan Wang,[a] Kai Xia,[a] Robert L. Z. Hoye,[b] Vincenzo Pecunia[‡a*]

[a] Institute of Functional Nano & Soft Materials (FUNSOM), Jiangsu Key Laboratory for Carbon-Based Functional Materials & Devices, Soochow University, 199 Ren'ai Road, Suzhou, 215123, Jiangsu, PR China. E-mail: vp293@suda.edu.cn

[b] Department of Materials, Imperial College London, Exhibition Road, London SW7 2AZ, United Kingdom.

‡ F. L. and V. P. contributed equally to this work.

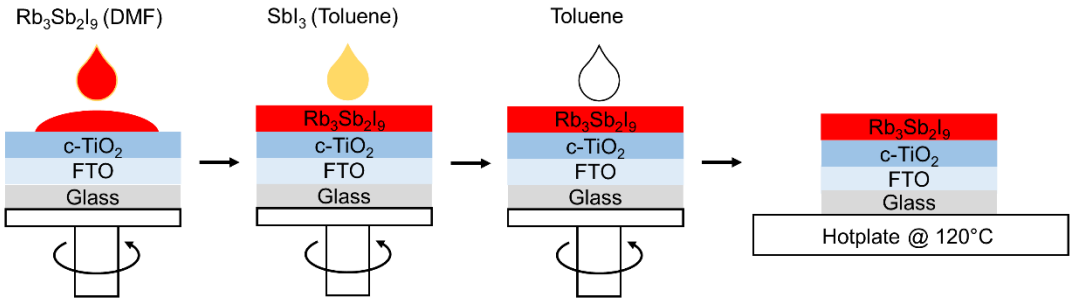

Figure S1 Conventional process (CP) referred to in the main text for the deposition of $Rb_3Sb_2I_9$ films. Here, antisolvent processing is carried out in two steps: firstly by dripping a dilute SbI_3 solution in toluene to compensate for iodine deficiency (*SbI_3:toluene dripping*), and then by dripping pure toluene to remove any excess SbI_3 (*toluene washing*). This is followed by a simple hotplate annealing.

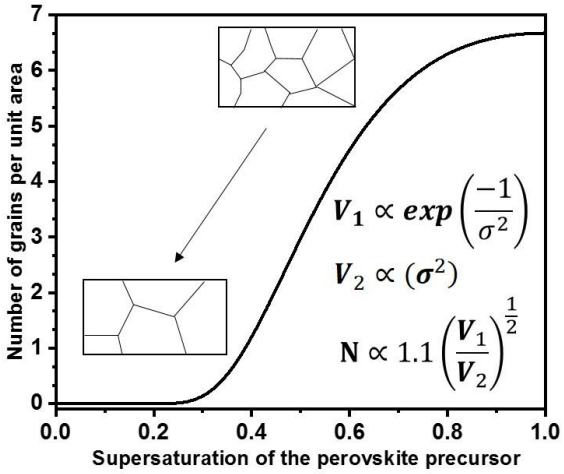

Figure S2 Relationship between grain size and supersaturation. V_1: crystal nucleation rate; V_2: crystal growth rate; σ: supersaturation level of the perovskite precursor; N: number of grains per unit area.[1] In nucleation theory,[2] the nucleation rate (V_1) is an exponential function of the supersaturation level (σ). On the other hand, according to the Burton-Cabrera-Frank (BCF) theory[3] at the low supersaturation levels, the crystal growth rate is a square function of the supersaturation level (σ). The resulting number of grains per unit area (N) reflects the combined effect of V_1 and V_2.

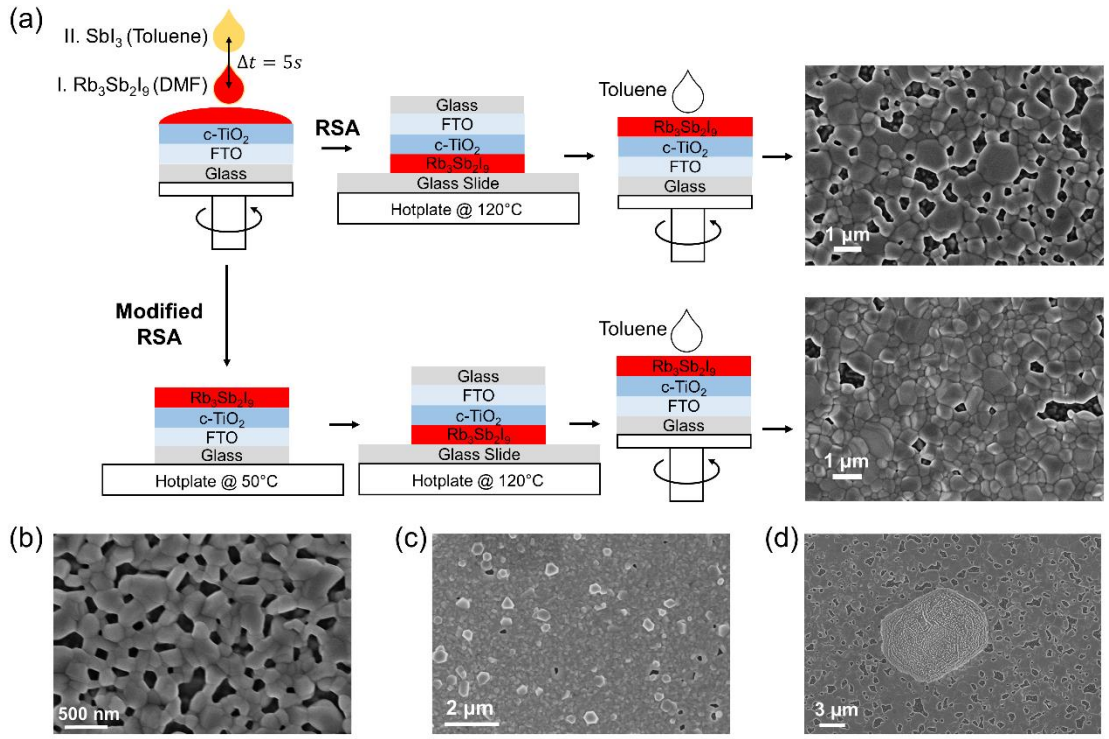

Figure S3 Basic RSA and modified RSA. (a) Schematic depiction of basic RSA and modified RSA, and SEM images of the resulting films. As discussed in the main text, the two types of RSA build on CP, differing from the latter mainly in regard to the hotplate annealing step, which is conducted with the sample turned over onto a glass slide so as to reduce the solvent evaporation rate. In addition, modified RSA features a straightforward hotplate annealing step at 50 °C prior to RSA proper, so as to limit the amount of solvent available when the sample is finally capped. We note that the glass substrates used for capping during RSA/modified RSA do not stick to the $Rb_3Sb_2I_9$ films. (b) SEM image of a film obtained when antisolvent processing in RSA is carried out as in CP (sequential *SbI_3:toluene dripping* and *toluene washing*): small domains and a large number of pinholes are formed. This can be attributed to the large amount of antisolvent left in the film during the annealing step, which disturbs grain growth. (c) SEM image of a film obtained when no antisolvent processing is carried out in RSA: small domains are formed, as likely determined by iodine deficiency. (d) SEM image of a large crystal-like feature on the film surface, obtained when RSA is conducted with only *SbI_3:toluene dripping* but no *toluene washing*. Features such as this come along with nearly pinhole-free films and large domain size. Such features, however, can be easily removed by dripping pure toluene *after* the annealing step of RSA, which leads to the modified RSA process flow shown in (a).

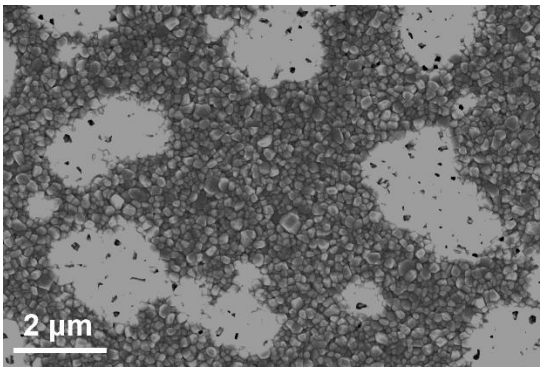

Figure S4 SEM images of film obtained via 225°C annealing without SbI_3 vapor assisted.

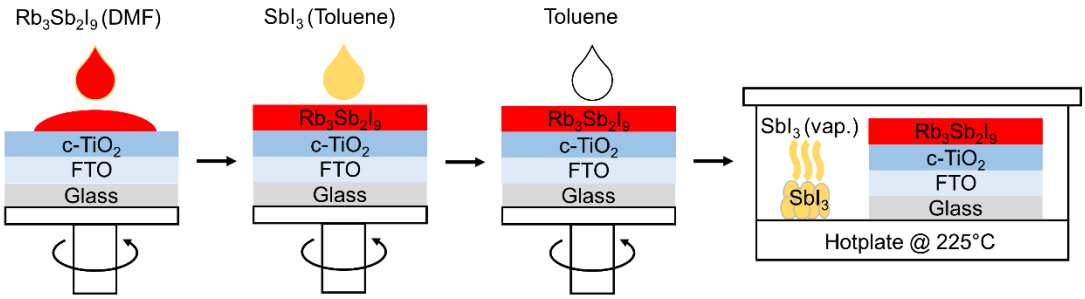

Figure S5 Schematic depiction of the HTVA process flow.

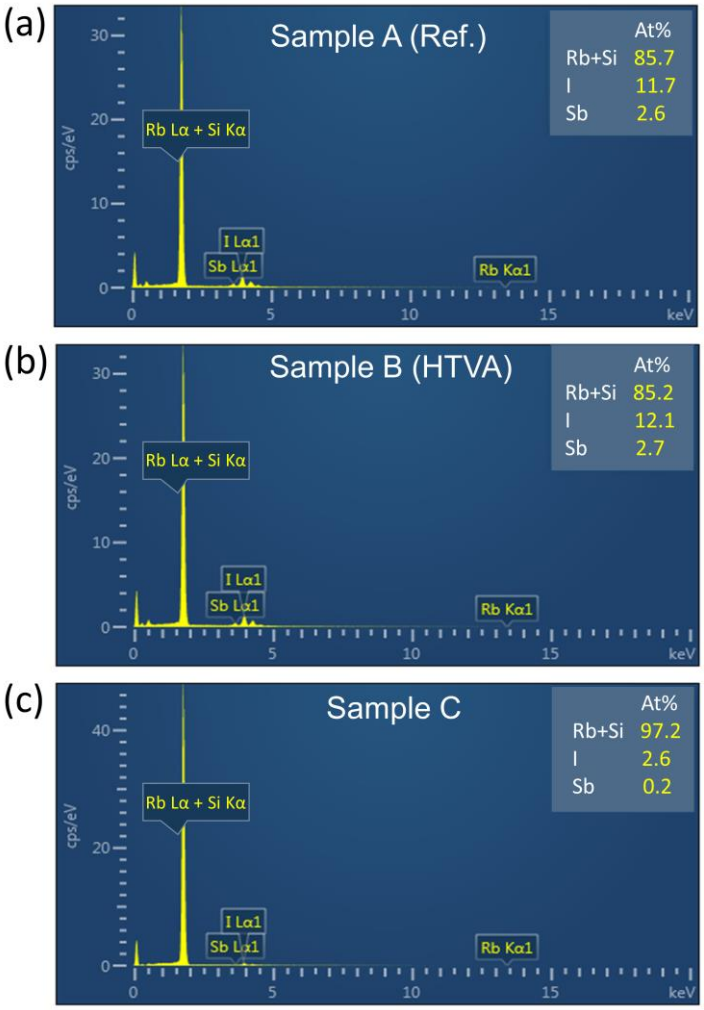

Figure S6 Energy-dispersive X-ray spectroscopy (EDS) of films processed through different methods. (a) Reference sample processed via CP and not subjected to high-temperature annealing (Sample A). (b) Sample annealed at 225 °C in SbI_3 vapor (HTVA; Sample B). (c) Sample annealed at 225 °C but not exposed to SbI_3 vapor (Sample C). All samples were fabricated on Silicon substrates.

Table S1 Values of the Sb/I ratio measured by EDS from the samples presented in Figure S6.

	Sb/I ratio
Sample A (reference)	0.222
Sample B (HTVA)	0.223
Sample C	0.077
Expected	0.222

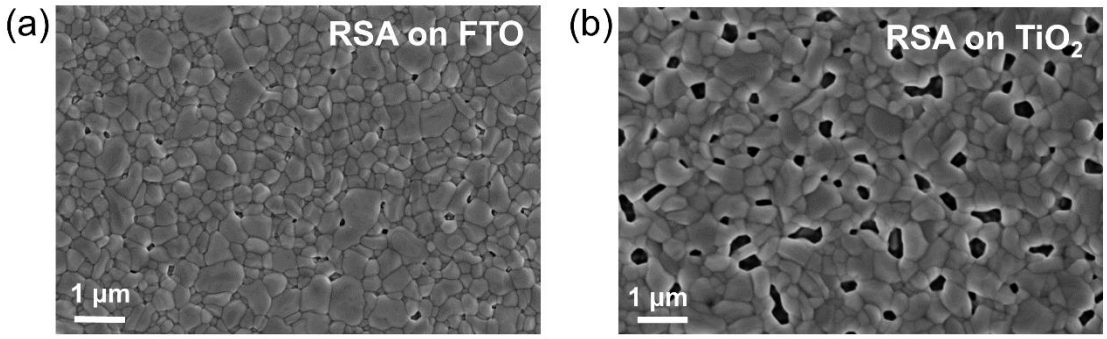

Figure S7 SEM images of RSA films on (a) FTO- and on (b) TiO_2-coated substrates.

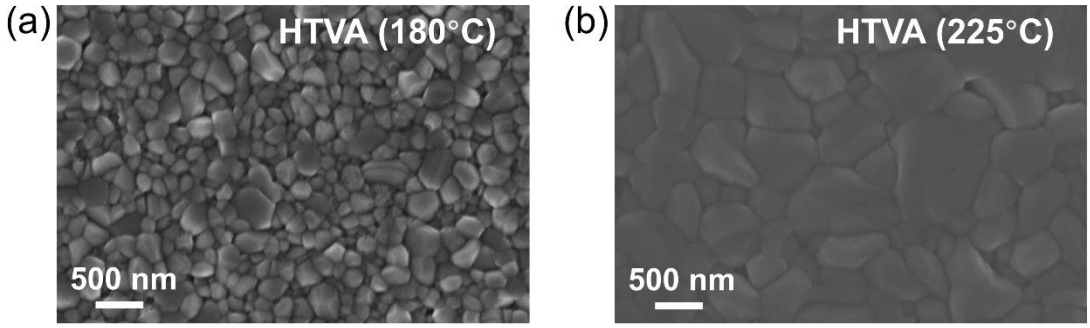

Figure S8 SEM images of films obtained via HTVA (a) at 180 °C and (b) at 225 °C.

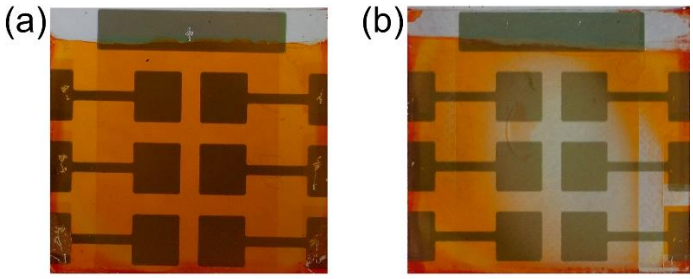

Figure S9 Photographs of samples in which $Rb_3Sb_2I_9$ was processed via HTVA at different annealing temperatures: (a) 225 °C; (b) 250 °C.

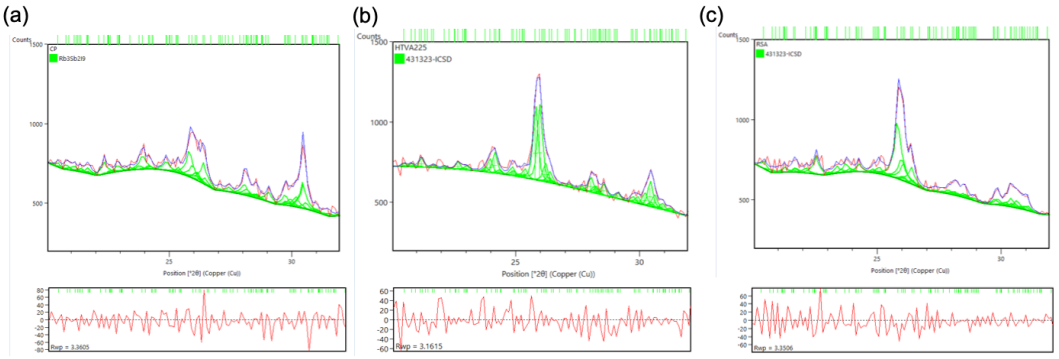

Figure S10. Diffraction patterns of $Rb_3Sb_2I_9$ films grown by the (a) conventional process, (b) high-temperature vapor annealing and (c) reduced supersaturation annealing methods. The patterns were fit using Pawley's method and the residuals are shown below.

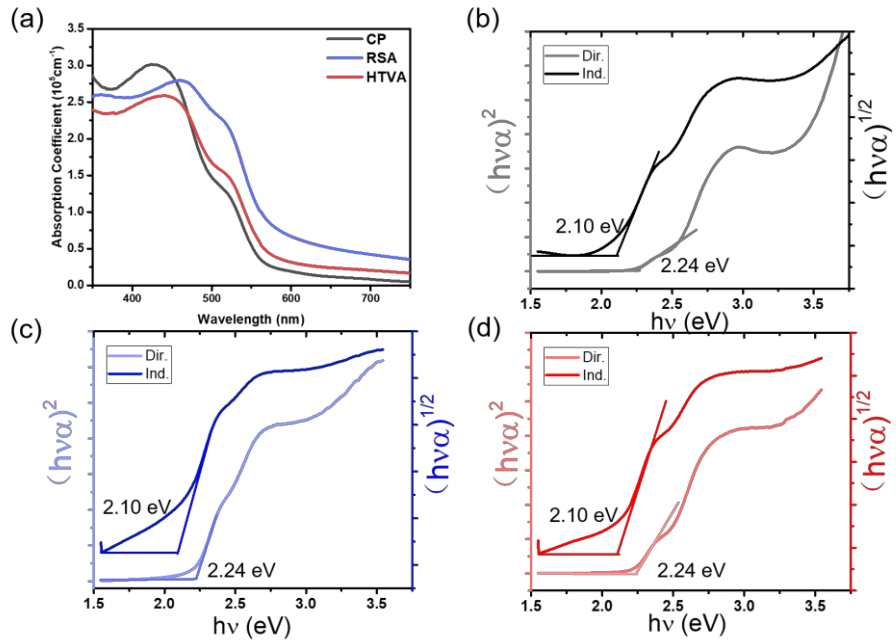

Figure S11 (a) Absorption coefficient of CP, RSA, HTVA films determined from absorbance data. Tauc plots of $Rb_3Sb_2I_9$ films deposited by (b) CP, (c) RSA, and (d) HTVA.

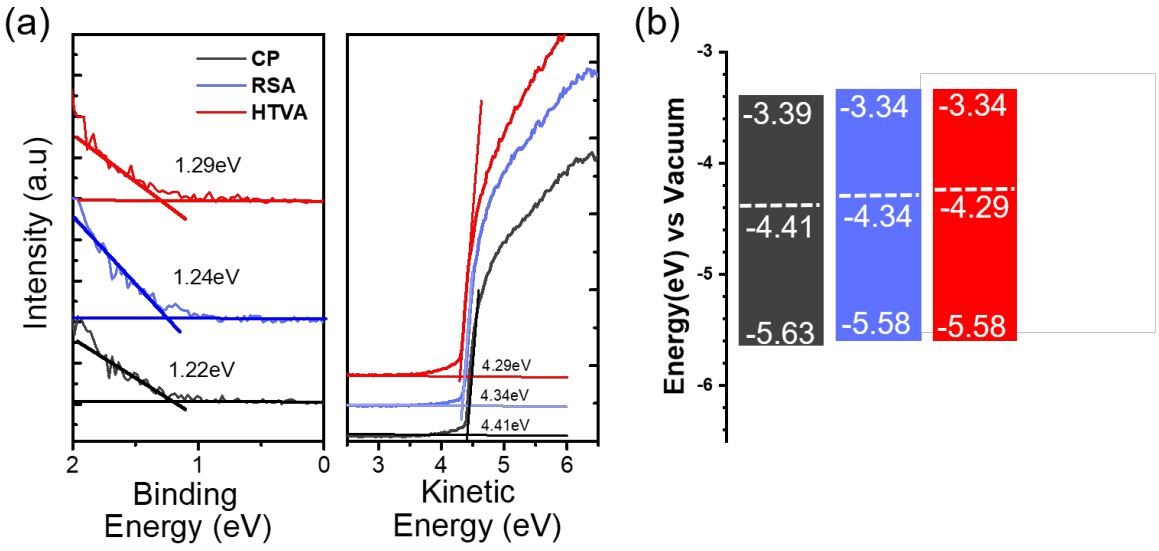

Figure S12 (a) UPS intensity from $Rb_3Sb_2I_9$ films: valence band states (left) and He I secondary electron cutoff (right). (b) Energy level diagrams derived from UPS and UV-Vis absorption data, under the approximation of negligible excitonic effects.

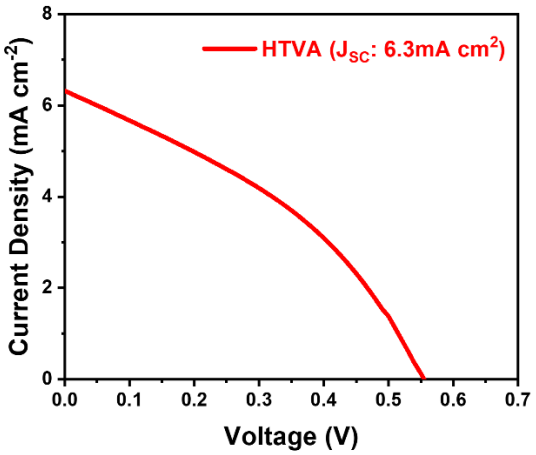

Figure S13 Measured current–voltage characteristic of a HTVA $Rb_3Sb_2I_9$ devices giving a short-circuit current density of 6.3 mA cm^{-2} under AM1.5G illumination.

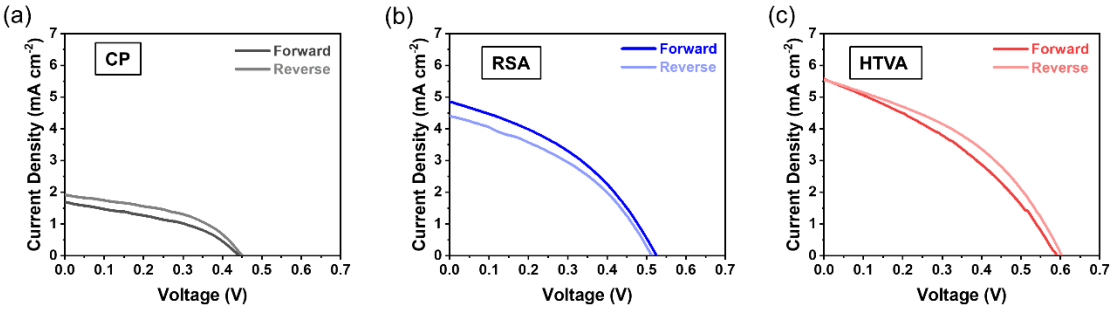

Figure S14 Double-sweep current–voltage characteristics of $Rb_3Sb_2I_9$ devices under AM1.5G illumination: (a) CP (H_{index} = 0.225); (b) RSA (H_{index} = -0.108); (c) HTVA (H_{index} = 0.126). The hysteresis index H_{index} is calculated as ($PCE_{Reverse}$ - $PCE_{Forward}$)/$PCE_{Reverse}$.[4]

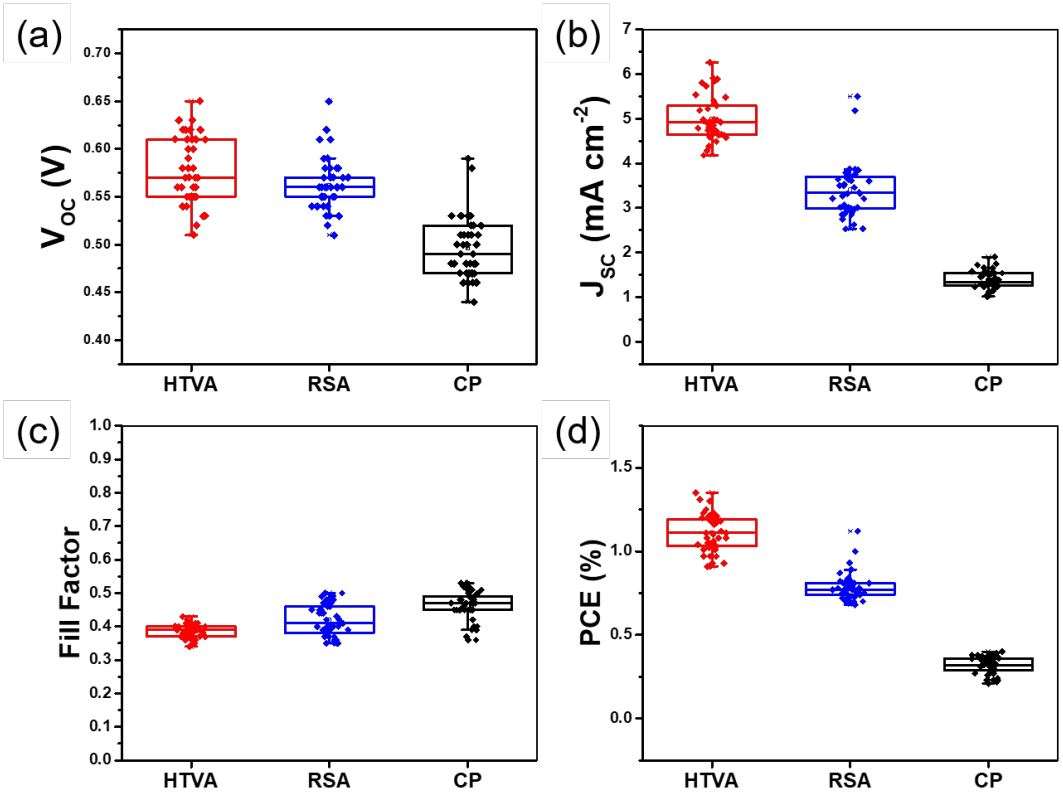

Figure S15 Photovoltaic parameter distribution of the different types of $Rb_3Sb_2I_9$ devices investigated in this work (40 devices of each sample type): (a) V_{oc}; (b) J_{sc}; (c) Fill Factor; (d) PCE.

Table S2 Performance of solar cells based on Bi- and Sb-halide perovskite derivatives (i.e., $A_3M_2X_9$, A^+: organic/inorganic cation, M: Sb^{3+}/Bi^{3+}, X^-: halide anion) from the literature.

Active layer	Device Structure	V_{oc} (V)	J_{sc} (mA cm^{-2})	FF (%)	PCE (%)	EQE_{max} (%)	Ref
$MA_3Bi_2I_9$	inverse	0.83	1.39	34	0.39	23	[5]
$MA_3Bi_2I_9$	mesoporous	1.01	4.02	78	3.17	48	[6]
$MA_3Bi_2I_9$	mesoporous	0.67	1.00	60	0.42	25	[7]
$MA_3Bi_2I_9$	mesoporous	0.65	1.1	50	0.36	No data	[8]
$MA_3Bi_2I_9$	mesoporous	0.51	0.94	61	0.31	28	[9]
$MA_3Bi_2I_9$	mesoporous	0.56	0.83	49	0.26	4.6	[10]
$MA_3Bi_2I_9$	mesoporous	0.68	0.52	33	0.12	12	[11]
$MA_3Bi_2I_9$	regular	0.72	0.49	32	0.11	17	[12]
$MA_3Bi_2I_9$	mesoporous	0.35	1.16	0.46	0.19	22	[13]
$MA_3Bi_2I_9$	inverse	0.66	0.22	0.49	0.07	No data	[14]
$MA_3Bi_2I_9$	mesoporous	0.84	0.17	35	0.05	4.0	[15]
$MA_3Bi_2I_9$	mesoporous	0.83	3.00	79	1.64	60	[16]
$MA_3Bi_2I_9$	mesoporous	0.87	2.7	69	1.62	25	[17]
$C_5H_6NBiI_4$	mesoporous	0.62	2.71	54	0.9	No data	[18]
$(C_6H_5NH_3)BiI_4$	mesoporous	0.58	6.03	22	0.78	No data	[19]
$Cs_3Bi_2I_9$	mesoporous	0.31	3.4	38	0.4	25	[20]
$Cs_3Bi_2I_9$	mesoporous	0.85	2.15	60	1.09	37	[11]
$Cs_3Bi_2I_9$	regular	0.86	5.78	64	3.2	56	[21]
$MA_3Sb_2I_9$	inverse	0.90	1.00	55	0.49	13	[22]
$MA_3Sb_2I_9$	inverse	0.62	5.41	61	2.04	21	[23]
$MA_3Sb_2I_9$	inverse	0.70	6.64	60	2.77	26	[24]
$Cs_3Sb_2I_9$	inverse	0.60	2.91	48	0.84	18	[23]
$Cs_3Sb_2I_9$	inverse	0.68	5.31	39	1.49	39	[25]

References

1 D. Liu, W. Zhou, H. Tang, P. Fu and Z. Ning, *Sci. China Chem.*, 2018, **61**, 1278–1284.

2 A. E. Nielsen, *Kinetics of precipitation*, Pergamon, 1964, vol. 18.

3 W.-K. Burton, N. Cabrera and F. C. Frank, *Philos. Trans. R. Soc. London. Ser. A, Math. Phys. Sci.*, 1951, **243**, 299–358.

4 Q. Jiang, Y. Zhao, X. Zhang, X. Yang, Y. Chen, Z. Chu, Q. Ye, X. Li, Z. Yin and J. You, *Nat. Photonics*, 2019, **13**, 460–466.

5 C. Ran, Z. Wu, J. Xi, F. Yuan, H. Dong, T. Lei, X. He and X. Hou, *J Phys Chem Lett*, 2017, **8**, 394–400.

6 S. M. Jain, D. Phuyal, M. L. Davies, M. Li, B. Philippe, C. De Castro, Z. Qiu, J. Kim, T. Watson, W. C. Tsoi, O. Karis, H. Rensmo, G. Boschloo, T. Edvinsson and J. R. Durrant, *Nano Energy*, 2018, **49**, 614–624.

7 X. Zhang, G. Wu, Z. Gu, B. Guo, W. Liu, S. Yang, T. Ye, C. Chen, W. Tu and H. Chen, *Nano Res.*, 2016, **9**, 2921–2930.

8 S. S. Mali, H. Kim, D.-H. Kim and C. Kook Hong, *ChemistrySelect*, 2017, **2**, 1578–1585.

9 A. Kulkarni, T. Singh, M. Ikegami and T. Miyasaka, *RSC Adv.*, 2017, **7**, 9456–9460.

10 T. Singh, A. Kulkarni, M. Ikegami and T. Miyasaka, *ACS Appl. Mater. Interfaces*, 2016, **8**, 14542–14547.

11 B. W. Park, B. Philippe, X. Zhang, H. Rensmo, G. Boschloo and E. M. Johansson, *Adv Mater*, 2015, **27**, 6806–6813.

12 M. Abulikemu, S. Ould-Chikh, X. Miao, E. Alarousu, B. Murali, G. O. Ngongang Ndjawa, J. Barbé, A. El Labban, A. Amassian and S. Del Gobbo, *J. Mater. Chem. A*, 2016, **4**, 12504–12515.

13 M. Lyu, J.-H. Yun, M. Cai, Y. Jiao, P. V Bernhardt, M. Zhang, Q. Wang, A. Du, H. Wang, G. Liu and L. Wang, *Nano Res.*, 2016, **9**, 692–702.

14 S. Öz, J.-C. Hebig, E. Jung, T. Singh, A. Lepcha, S. Olthof, F. Jan, Y. Gao, R. German, P. H. M. van Loosdrecht, K. Meerholz, T. Kirchartz and S. Mathur, *Sol. Energy Mater. Sol. Cells*, 2016, **158**, 195–201.

15 H. Li, C. Wu, Y. Yan, B. Chi, J. Pu, J. Li and S. Priya, *ChemSusChem*, 2017, **10**, 3994–3998.

16 Z. Zhang, X. Li, X. Xia, Z. Wang, Z. Huang, B. Lei and Y. Gao, *J Phys Chem Lett*, 2017, **8**, 4300–4307.

17 S. M. Jain, T. Edvinsson and J. R. Durrant, *Commun. Chem.*, , DOI:10.1038/s42004-019-0195-3.

18 T. Li, Y. Hu, C. A. Morrison, W. Wu, H. Han and N. Robertson, *Sustain. Energy Fuels*, 2017, **1**, 308–316.

19 X.-L. Li, L.-L. Gao, B. Ding, Q.-Q. Chu, Z. Li and G.-J. Yang, *J. Mater. Chem. A*, 2019, **7**, 15722–15730.

20 M. B. Johansson, H. Zhu and E. M. Johansson, *J Phys Chem Lett*, 2016, **7**, 3467–3471.

21 F. Bai, Y. Hu, Y. Hu, T. Qiu, X. Miao and S. Zhang, *Sol. Energy Mater. Sol. Cells*, 2018, **184**, 15–21.

22 J.-C. Hebig, I. Kühn, J. Flohre and T. Kirchartz, *ACS Energy Lett.*, 2016, **1**, 309–314.

23 K. M. Boopathi, P. Karuppuswamy, A. Singh, C. Hanmandlu, L. Lin, S. A. Abbas, C. C. Chang, P. C. Wang, G. Li and C. W. Chu, *J. Mater. Chem. A*, 2017, **5**, 20843–20850.

24 P. Karuppuswamy, K. M. Boopathi, A. Mohapatra, H.-C. Chen, K.-T. Wong, P.-C. Wang and C.-W. Chu, *Nano Energy*, 2018, **45**, 330–336.

25 A. Singh, K. M. Boopathi, A. Mohapatra, Y. F. Chen, G. Li and C. W. Chu, *ACS Appl Mater Interfaces*, 2018, **10**, 2566–2573.